Lecture 10: More applications

Edgar Knobloch: notes by Duncan Hewitt and Pedram Hassanzadeh
with substantial editing by Edgar Knobloch

January 9, 2013

1 The Swift-Hohenberg Equation as a Model

The Swift-Hohenberg equation has proved to be a very useful model system for studying the properties of spatially localized structures in physical systems. This is because of the following properties:

- The equation is fourth order in the spatial variables
- The equation has an intrinsic length scale $2\pi/q_c$
- The equation is spatially reversible
- The equation exhibits bistability due to competing nonlinear terms
- The equation is relatively easy to analyze, at least in one dimension.

The main reason the equation can be understood in such detail is a consequence of the spatial reversibility and the fact that it can be written as a variational problem,

$$u_t = -\frac{\delta F}{\delta u} \quad \text{where} \quad F = \int_{-\infty}^{\infty} \mathrm{d}x \left[-\frac{1}{2} r u^2 + \frac{1}{2} \left[\left(q_c^2 + \frac{\partial^2}{\partial x^2} \right) u \right]^2 - \int_0^u f(v) dv \right]. \qquad (1)$$

In this section we consider the symmetries of the Swift-Hohenberg equation in one spatial dimension, and examine the effects of breaking some of these symmetries. In the following sections we will use these results as a basis for examination of more complex systems, such as those arising in fluid mechanics.

1.1 Two Cases: SH23 and SH35

We first look at two cases of the Swift-Hohenberg equation with different nonlinear terms, and different corresponding symmetries, namely, SH23 and SH35.

SH23 has $f(u) = b_2 u^2 - u^3$ and the following reflection and translational symmetries:

- $R_1 : x \longrightarrow -x, \qquad u \longrightarrow u$
- $T : x \longrightarrow x + d, \qquad u \longrightarrow u.$

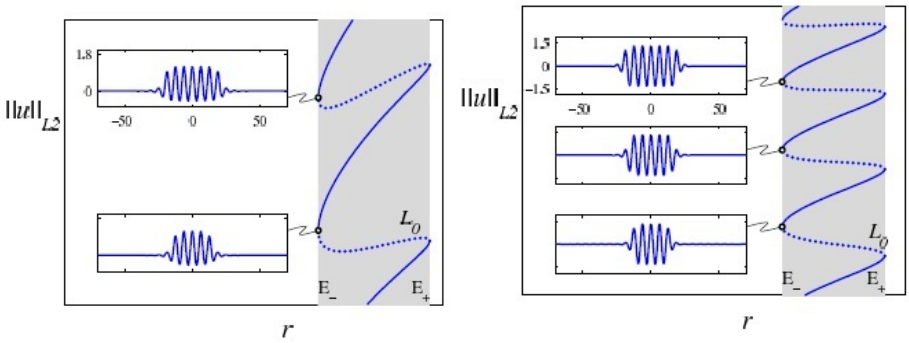

(a) SH23 (b) SH35

Figure 1: Growth along the L_0 branch of states with even symmetry. The pinning region is shaded. (a) SH23. (b) SH35. From [3].

As a result there are two types of localized solutions, those fixed by R_1 (even states L_0, L_π), and asymmetric "rung" states with no symmetry, together with their translates.

SH35 has $f(u) = b_3u^3 - u^5$ and the following reflection and translational symmetries:

- $R_1 : x \longrightarrow -x, \qquad u \longrightarrow u$
- $R_2 : x \longrightarrow x, \qquad u \longrightarrow -u$
- $T : x \longrightarrow x + d, \qquad u \longrightarrow u.$

As a result there are three types of localized solutions: those fixed by R_1 (even states L_0, L_π) and their translates; those fixed by $R_1 \circ R_2$ (odd states $L_{\pi/2}$, $L_{3\pi/2}$) and their translates, and asymmetric "rung" states. It is important to observe that L_0 and L_π are related by R_2, and likewise for $L_{\pi/2}$, $L_{3\pi/2}$. Consequently the bifurcation diagram in Fig. 1(b) contains only a single branch of even states and a single branch of odd states.

Figure 1 compares the growth along the L_0 branches in SH23 and SH35 and shows that SH35 has twice as many turns compared to SH23. It is therefore of interest to explore what happens when the symmetry R_2 of SH35 is progressively broken. How does the snaking branch in Fig. 1(b) deform into the snaking branch in Fig. 1(a)? What are the consequences of this process?

1.1.1 Variational case

To study the effect of breaking the R_2 symmetry in SH35, we add a term ϵu^2 to the right-hand side SH35,

$$u_t = ru - (1 + \partial^2/\partial x^2)^2 u + b_3 u^3 - u^5 + \epsilon u^2. \tag{2}$$

When $\epsilon \neq 0$ this equation, like SH23, possesses only R_1 and T symmetries, and hence the only symmetric states are L_0, L_π. The odd parity states $L_{\pi/2}$, $L_{3\pi/2}$ become states with no symmetry and reconnect with the rung states forming two different types of branches: S branches and Z branches [8]. Figure 2 shows the effect of breaking the R_2 symmetry (for $\epsilon = 0.03$).

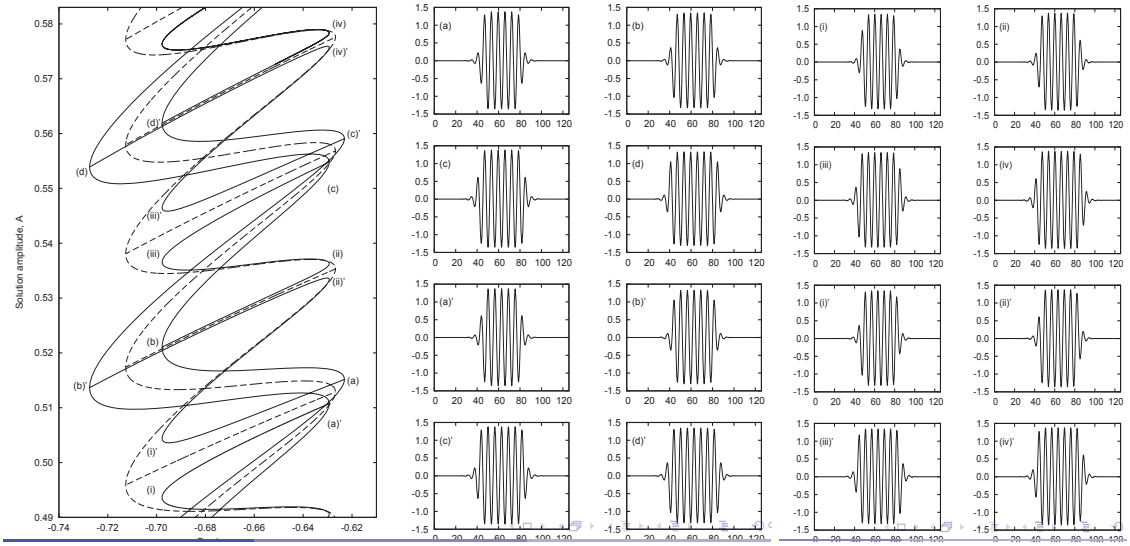

Figure 2: The snakes-and-ladders structure in the variational case with $\epsilon = 0.03$ and $b_3 = 2$. The solution branches for $\epsilon = 0$ are shown dashed. For $\epsilon \neq 0$ the even parity branch splits into two distinct even parity states L_0 and L_π, while the odd parity states reconnect with original "rung" states forming pairs of disconnected branches of asymmetric states referred to as S and Z branches. The solutions $u(x)$ at the saddle nodes: (a)–(d) are from the L_π branch, and (a')–(d') are from the L_0 branch. (i)–(iv) are solutions at the saddle-nodes on the S branches, and (i')–(iv') are from the Z branches. From [8].

Figure 3 shows the effect of increasing ϵ for the variational case (2). Both symmetric and asymmetric states are stationary, and the Z branches are stretched by increasing ϵ.

1.1.2 Nonvariational case

We can also break the R_2 symmetry by adding the term $\epsilon(\partial u/\partial x)^2$ to SH35. The new equation, i.e.,

$$u_t = ru - (1 + \partial^2/\partial x^2)^2 u + b_3 u^3 - u^5 + \epsilon(\partial u/\partial x)^2, \tag{3}$$

is not variational, i.e., it cannot be written in the form (1). The effect of increasing ϵ in this case is qualitatively similar to the variational case. However, here the asymmetric states are no longer stationary, as shown in Fig. 4.

Because (asymmetric) states are now nonstationary, we can consider the effect of collisions between two such states. Figure 5(a) shows a collision between two identical localized states drifting in opposite direction. The result is a symmetric (and, therefore, stationary) state. In contrast, Figs. 5(b)–5(e) show that collisions of nonidentical states can lead to other types of behavior. The collisions result in either stationary (symmetric) states or moving (asymmetric) states. The outcome of the collision is determined in general by the shape of the approaching fronts – whether these are like (in phase) or unlike (out of phase). See Figs. 5(b)–5(e) and [8] for more details.

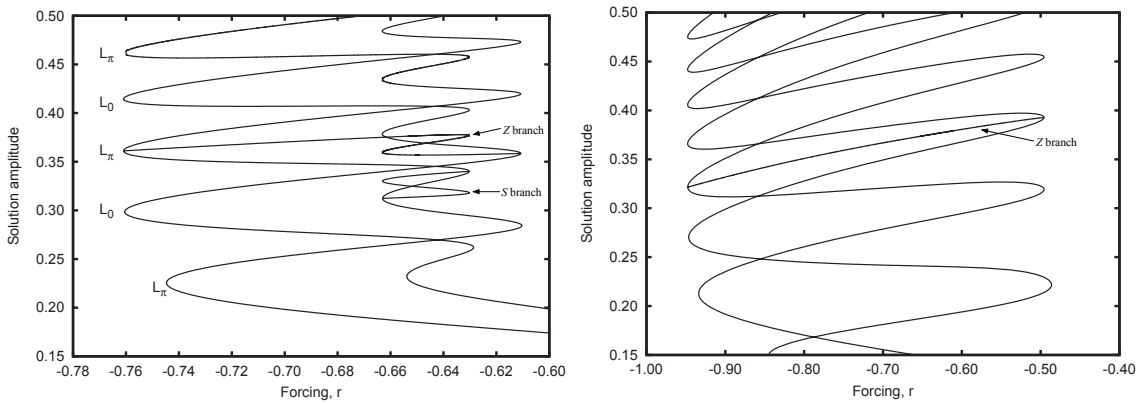

(a) $\epsilon = 0.1$ (b) $\epsilon = 0.5$

Figure 3: The effect of increasing ϵ in the variational case, with $b_3 = 2$: only one S and one Z branch is shown. In (b) the S branch has vanished and the Z branch has straightened out. From [8].

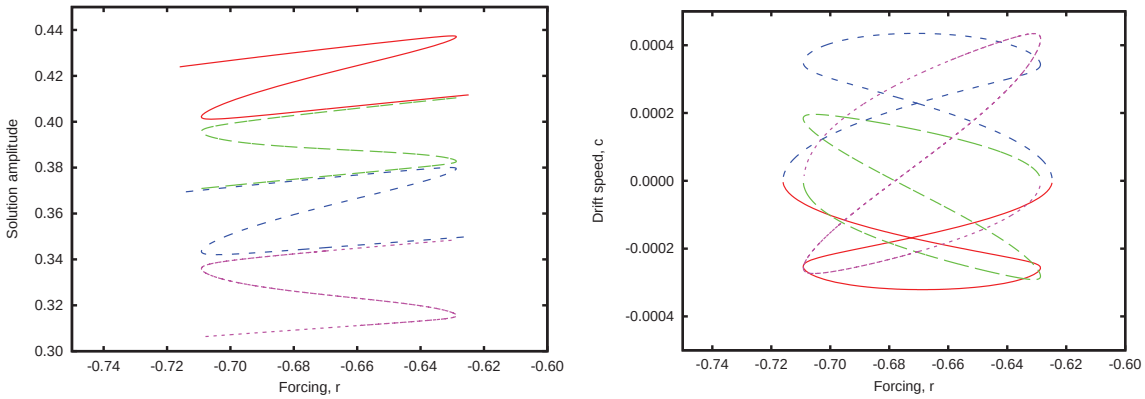

(a) (b)

Figure 4: (a) The S and Z branches in the nonvariational case when $\epsilon = 0.01$ and $b_3 = 2$. (b) The corresponding drift speed c; when $\epsilon \neq 0$ c is generically nonzero although it can vanish at isolated values of the bifurcation parameter r. From [8].

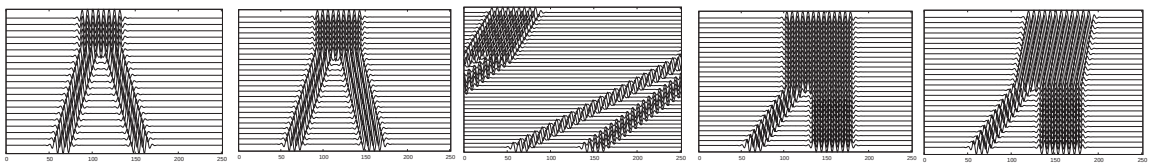

(a) (b) (c) (d) (e)

Figure 5: Space-time diagrams showing the collision of different states, for $r = -0.65$, $b_3 = 2$ and $\epsilon = 0.1$: (a) two identical states, resulting in a symmetric state; (b)–(e) nonidentical collisions, resulting in either symmetric (stationary) or asymmetric (moving) localized states. Time increases upward. From [8].

In all cases the collisions are inelastic and the length of the final state exceeds the combined length of the colliding states. This is a consequence of the fact that additional nucleation events take place just before the collision.

2 Applications

We now briefly consider the relevance of the Swift–Hohenberg results to several physical systems. Specifically we consider (1) collisions between convectons, and (2) 'multipulse' states (multiple localized states in the domain) in systems which share the symmetry properties of the Swift-Hohenberg equation, but not its variational behavior.

2.1 Binary fluid convection

Two-dimensional binary-fluid convection was discussed in lecture 9. In particular lecture 9 described in some detail the properties of spatially localized solutions termed convectons. We use this same system now to generate moving convectons. To do so we relax the midplane symmetry of the system that was imposed through the use of the Boussinesq approximation and of identical boundary conditions at top and bottom. In the following we retain the Boussinesq approximation and imagine the top and bottom boundaries in contact with appropriate heat baths, of temperature T_U and T_L, respectively, with flux boundary conditions

$$\frac{dT_-}{dz} = -\frac{B_-}{d}\,(T_L - T_-) \qquad \text{at} \qquad z = 0, \tag{4}$$

$$\frac{dT_+}{dz} = -\frac{B_+}{d}\,(T_+ - T_U) \qquad \text{at} \qquad z = l, \tag{5}$$

where l is the depth of the layer, T_+ and T_- are the temperatures immediately outside the upper and lower heat baths (which vary in time), and $B_\pm$ are the Biot numbers of the boundaries: $B = 0$ corresponds to insulating boundaries, while $B = \infty$ corresponds to pure conducting boundaries. The key observation here is that, if $B_+ \neq B_-$, these boundary conditions mark a departure from the symmetric conditions imposed in lecture 9.

The system is characterized by cross-diffusion such that the concentration field is coupled to the temperature field: the effects of this coupling are described by a separation ratio S.

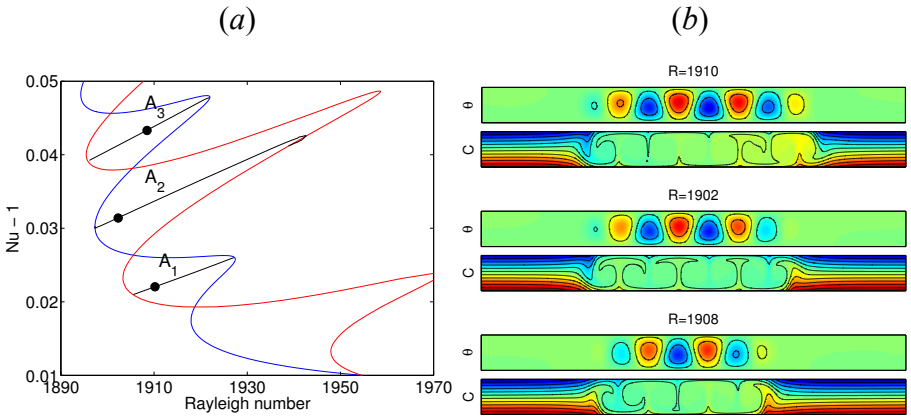

Figure 6: (a) Bifurcation diagram for $\beta = 1$ showing odd (blue curve) and even (red curve) states together with the asymmetric states (black curves). (b) Contours of constant temperature fluctuation (upper panels) and concentration (lower panels) for traveling convectons on the rungs of the snakes-and ladders bifurcation diagram. The location of each state is indicated by dots in (a). Parameters: $S = -0.1$, $\sigma = 7$, and $\tau = 0.01$. From [12].

Here (as in lecture 9) we assume that $S < 0$, such that the heavier molecular weight fluid migrates up the temperature gradient, towards the hotter bottom boundary. As a result we have bistability between the background conduction state and the periodic convecting state. The brief overview that follows is based on [12], where further details may be found.

In order to characterize the amplitude of convection and construct a bifurcation diagram we must define a parameter that characterizes the system, i.e., we need a parameter that remains fixed even during time-dependent evolution of the system. The usual Rayleigh number, defined in terms of the temperature drop ΔT across the fluid layer, is inappropriate as soon as the temperature of the boundaries can change in response to the heat deposited by flow, in other words, as soon as the boundaries fail to be perfectly conducting. For this purpose we define the Rayleigh number Ra in terms of the temperature difference $\Delta T'$ across the layer *in the conduction state* [12]. When the boundaries are perfectly thermally conducting this definition reduces to the usual definition. We also define the Prandtl number $\sigma = \nu/\kappa$, the ratio of viscosity to thermal diffusivity, and the Lewis number $\tau = D/\kappa$, the ratio of compositional to thermal diffusivity. In the following we assume that the lower boundary is perfectly conducting ($B_- = \infty$) and suppose that the upper boundary is characterized by a finite Biot number B_+. Under these conditions the thermal boundary conditions (4) and (5), written in terms of dimensionless variables, become

$$(1-\beta)\,\theta_z + \beta\theta = 0 \quad \text{on} \quad z = 1, \qquad \theta = 0 \quad \text{on} \quad z = 0, \tag{6}$$

where θ is the dimensionless departure of the temperature from its conduction profile. Here β is the effective Biot number of the upper boundary and is given by $\beta \equiv B_+/(1+B_+)$. We also impose no-slip impenetrable boundary conditions on the upper and lower boundaries. It follows that $\beta = 1$ implies that the system is symmetric, with a perfectly conducting boundary at $z = 1$ as well as $z = 0$. If instead $\beta = 0$, the upper boundary is perfectly

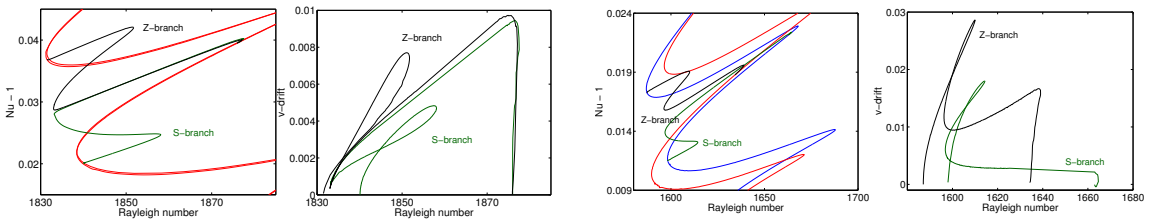

(a) $\beta = 0.95$ (b) $\beta = 0.5$

(c) $\beta = 0.3$ (d) $\beta = 0$

Figure 7: Left panels: bifurcation diagrams showing the even parity states generated by splitting of the $\beta = 1$ even states and the S and Z states resulting from the reconnection between the $\beta = 1$ odd states and the asymmetric rung states, for different values of β. Right panels: velocity c of the S and Z states. The parameter values are given in Fig. 6. From [12].

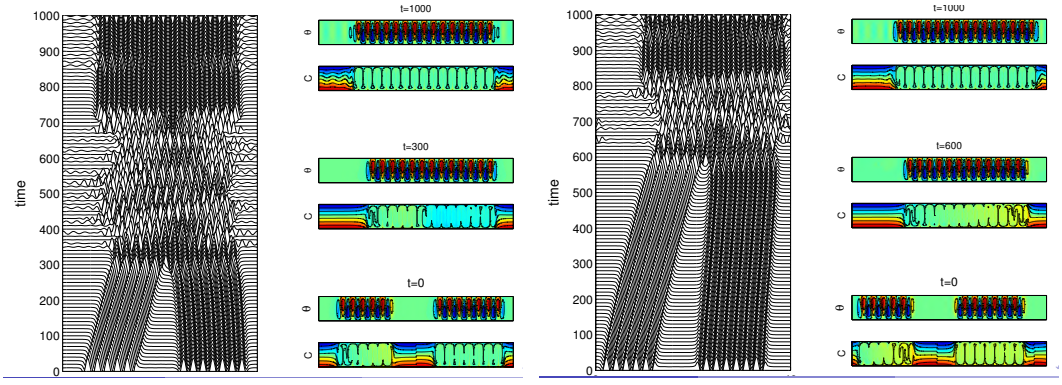

(a) (b)

Figure 8: Space-time plots showing two different collisions of two states, with S =-0.5, $\beta = 0.9$, $\sigma = 0.6$, $\tau = 0.03$, and $Ra = 2750$. The collisions result in complex dynamics and the generation of waves, and ultimately end up in a symmetric state higher up the snaking branch than either of the initial states. From [12].

insulating. Thus the departure of β from $\beta = 1$ provides a measure of the magnitude of the breaking of the midplane reflection symmetry in this system.

It follows that when $\beta = 1$, the system has a midplane symmetry, and we then expect that both odd and even solutions are present and stationary. Figure 6(a) shows the resulting snakes-and-ladders bifurcation diagram and reveals that the asymmetric rung states now drift (Fig. 6(a)). This is a consequence of the absence of variational structure of the equations. Three of the resulting drifting convectons are shown in Fig. 6(b).

When $\beta < 1$ the midplane symmetry is absent, and the snakes-and-ladders structure of the pinning region breaks up. The odd parity solutions and the rung states become drifting S and Z states, just as in the case of SH35 with a nonvariational R_2 symmetry-breaking term. Figure 7 shows the bifurcation diagrams for a sequence of different values of $\beta < 1$ as specified below each pair of panels. The even parity solutions have split into two, and the new S and Z states now drift. One can check [12] that the Z branch connects the two even parity branches produced by the splitting of the even parity states while the S branch connects an even parity branch to itself. The corresponding speeds of the S and Z states are shown in Fig. 7(b).

Since some of states now move we can study collisions between them by direct numerical integration in time, just as in the Swift-Hohenberg equation. The nice thing about generating moving convection by breaking the midplane symmetry is that in principle one has access to multiple drifting states of different lengths, all of which are simultaneously stable. However, it turns out that for the parameter values used in lecture 9 the drifting convectons are unstable. This is no longer so for the parameter values characteristic of liquid ^{3}He-^{4}He mixtures and in Fig. 8 we show two of the resulting collisions [12]. Unlike the Swift-Hohenberg equation, this system supports waves, and the collisions result in complex dynamics. However, ultimately a new symmetric state is formed with a greater width than either of the incident convectons, just as in the Swift-Hohenberg equation.

The correspondence between the behavior of this complex physical system and the corresponding behavior in the Swift-Hohenberg equation is striking. The reason that the Swift-Hohenberg equation is so successful at describing complex systems of this type is ultimately due to the presence of a tangency between the unstable manifold of a homogeneous state and the stable manifold of a periodic orbit. Once these manifolds intersect transversely as described in lecture 8 the intersections are robust and hence insensitive to (small) changes in parameter values, and indeed in the equations and boundary conditions themselves.

2.2 Binary fluid convection in a porous medium

Next we consider binary fluid convection in a two-dimensional fluid-saturated porous layer, characterized by porosity ϵ and a separation ratio S, which controls the separation between lighter and heavier components. Again, if $S < 0$ the heavier component migrates toward the hotter boundary. As in the bulk binary fluid convection case discussed in lecture 9, the competing effects of composition and temperature on the density lead to bistability between the background conduction state and a periodic convecting state. The discussion of the section is based on [10], to which the reader is referred for more information.

The flow $\boldsymbol{u} = (u, w)$ in the porous medium is described by Darcy's law and is incompressible, while the temperature T and concentration C satisfy advection-diffusion equations.

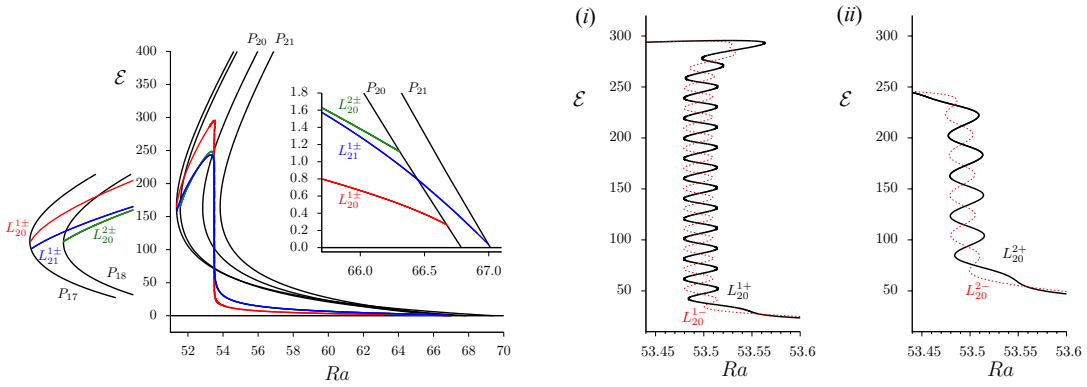

Figure 9: (a) Bifurcation diagram showing secondary branches of localized states connecting different periodic states. The inset shows enlargements of the behavior near the onset and termination of the secondary branches. The snaking region is not resolved on this plot. (b) The snaking region from (a), showing (i) examples of even (solid) and odd (dashed) single-pulse states, and (ii) equally spaced two-pulse states. The parameters are $\tau = 0.5$ and $S = -0.1$. From [10].

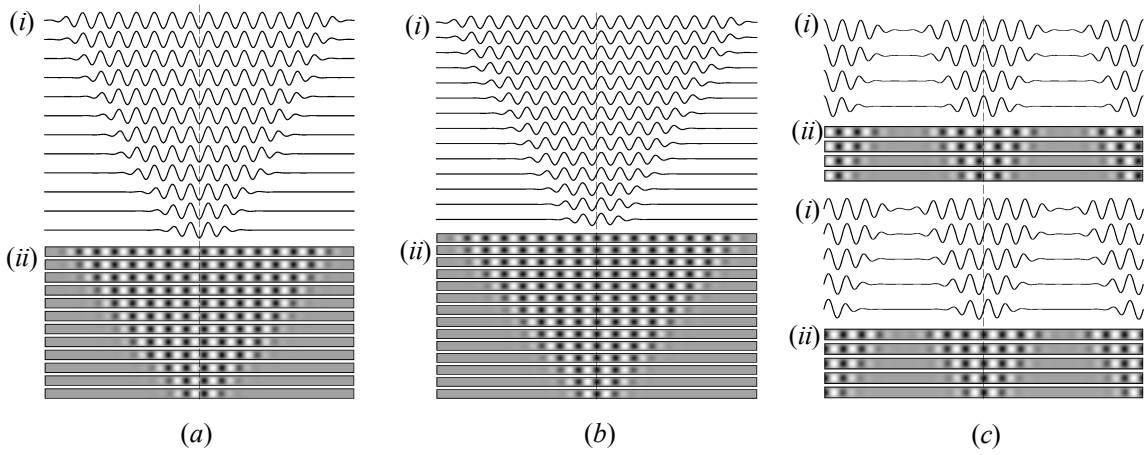

Figure 10: Line plots of the midplane vertical velocity w (i) and the streamfunction (ii) up the snaking region, for $\tau = 0.5$ and $S = -0.1$: (a) even parity state; (b) odd parity state; (c) even and odd states for two convectons. From [10].

These equations are given in dimensionless form by

$$\boldsymbol{u} = -\nabla p + Ra\,(T + SC)\,\boldsymbol{e}_z, \qquad \nabla \cdot \boldsymbol{u} = 0, \tag{7}$$

$$\partial_t T = -\,(\boldsymbol{u} \cdot \nabla)\,T + \nabla^2 T, \tag{8}$$

$$\epsilon \partial_t C = -\,(\boldsymbol{u} \cdot \nabla)\,C + \tau\left(\nabla^2 C - \nabla^2 T\right). \tag{9}$$

To obtain these equations we have used a linear equation of state $\rho = \rho_0(1 - \alpha(T - T_0) + \beta(C - C_0)$, where $\alpha > 0$ and $\beta > 0$ are the constant coefficients of thermal and compositional expansion, respectively. The dimensionless parameters are the Lewis number $\tau = D/\kappa$, the Rayleigh number $Ra = g\alpha\Delta T l/\lambda\kappa$, and the separation ratio $S = S_{\rm soret}\beta/\alpha < 0$. Here λ is the Darcy friction coefficient and l is the layer depth.

The boundary conditions are given by

$$w = T - 1 = (C - T)_z = 0 \qquad \text{at} \qquad z = 0, \tag{10}$$

$$w = T = (C - T)_z = 0 \qquad \text{at} \qquad z = 1, \tag{11}$$

and are periodic in the x direction with period Γ. We consider the departure from the base (conduction) state $T = 1 - z$, $C = 1 - z$, $\boldsymbol{u} = 0$, given by the variables $(\theta, \Sigma, \boldsymbol{u})$. The equations for these variables have important symmetry properties:

- Invariance under translations in x;
- Invariance under reflection with respect to $x = 0$ (R_1);
- Invariance under reflection with respect to $z = 1/2$ (R_2).

With periodic boundary conditions in the horizontal, these operations generate the symmetry group $O(2) \times Z_2$, and as a consequence we expect the equations to exhibit behavior that is qualitatively similar to that already described for SH35. Figure 9(a) demonstrates that this is indeed the case. The figure reveals the presence of several subcritical branches of periodic states of which the branch P_{20} sets in first. This is a consequence of choosing a periodic domain $\Gamma = 20$ for the computations. The figure also shows three pairs of secondary branches of localized states, all of which snake. In particular, the branches labeled $\mathrm{L}_{20}^{1\pm}$ bifurcate together from P_{20} at smallest amplitude and terminate together on P_{17}. The reason why on finite periodic domains the snaking branches may terminate on a different periodic state than the one they bifurcate from (or indeed on two different branches) can be traced to the Rayleigh number dependence of the wavelength within the localized structure as discussed in detail in [2]. Figure 10(a) shows the even parity states L_{20}^{1+} at successive left saddle-nodes proceeding up the snaking diagram while Fig. 10(b) shows similar results for the odd parity states L_{20}^{1-}. Both are single-pulse states in the sense that as $\Gamma \to \infty$ the phase space trajectory returns to the conduction after a single visit to a neighborhood of the limit cycle corresponding to the periodic state. In contrast, the branches $\mathrm{L}_{20}^{2\pm}$ bifurcate from P_{20} at larger amplitude (and terminate on P_{18}) because they are branches of equidistant two-pulse states (Fig. 10(c)). The states L_{20}^{2+} consist of a bound state of two identical even parity pulses in the domain Γ, while L_{20}^{2-} consists of a bound state of two identical odd parity pulses in Γ. Since the pulses are equidistant they behave exactly like

single-pulse states in a domain $\Gamma/2$ as seen in Fig. 9(a). As mentioned in lecture 7 this is no longer the case for unequally spaced two-pulse states which are located on isolas within the snaking region. In contrast, the two-pulse states L_{21}^{1+} bifurcating from the second primary branch P_{21} consist of a bound states of *opposite* even parity states, i.e., equidistant bound states of a pulse with a maximum in the middle and a pulse with a minimum in the middle. Similarly, L_{21}^{1-} are equidistant bound states of two opposite odd parity states (with opposite slopes on their centerline).

Lo Jacono et al [10] also study the various tertiary branches analogous to the rung states in standard homoclinic snaking but this time connecting the branches of two-pulse states. Related results based on SH23 are described in [9].

2.3 Rotating convection

For a different application, we look at the classical problem of rotating Rayleigh-Bénard convection in two dimensions [13]. For this problem, the governing equations are

$$\begin{aligned} Ra\,\theta_x - Ta\,v_z + \nabla^4\psi &= \sigma^{-1}\left[\nabla^2\psi_t + J(\psi,\nabla^2\psi)\right] && (12)\\ \psi_x + \nabla^2\theta &= \theta_t + J(\psi,\theta) && (13)\\ Ta\,\psi_z + \nabla^2 v &= \sigma^{-1}\left[v_t + J(\psi,\theta)\right], && (14) \end{aligned}$$

where the three-dimensional velocity field in the rotating frame is $\boldsymbol{u} = (-\psi_z, v, \psi_x)$ with poloidal streamfunction ψ, and $J(f,g) \equiv f_x g_z - f_z g_x$. Here $v(x,z,t)$ is the zonal velocity, θ is the departure of the temperature from the pure conduction profile $T = 1 - z$, $\sigma \equiv \nu/\kappa$ is the Prandtl number and $Ra \equiv g\alpha\Delta T l^3/\nu\kappa$ is the Rayleigh number, where ΔT is the temperature difference across a fluid layer of height l. The importance of rotation is measured by the Taylor number $Ta = 2\Omega l^2/\nu$ (inverse Ekman number), where Ω is the (constant) rotation rate about the vertical axis. Following [13], we use the stress-free boundary conditions at $z = 0, 1$,

$$\psi = \psi_{zz} = \theta = v_z = 0. \qquad (15)$$

With these boundary conditions

$$\frac{d\bar{V}}{dt} = 0, \quad \text{where} \quad \bar{V} \equiv \int_D v(x,z,t)\,dx\,dz\,, \qquad (16)$$

where D refers to the domain $[-\Gamma/2, \Gamma/2] \times [0,1]$. Thus the total zonal momentum $\bar{V}$ is a conserved quantity. See [1] for further details. The vertically averaged zonal momentum, $V(x) \equiv \int_0^1 v(x,z)dz$, satisfies

$$\sigma\,\frac{dV}{dx} = -\int_0^1 \psi_z v\,dz\,, \qquad (17)$$

implying that in steady states a horizontal zonal shear is balanced by the Reynolds stress on the right side of the equation. In the following we introduce the quantity $\Delta V \equiv V(x = L/2) - V(x = -L/2)$ that measures the zonal velocity difference across a convecton of length L. This is always anticyclonic, i.e., $\Delta V < 0$ (see Fig. 12 and 13).

Figure 11 shows the bifurcation diagrams for the average poloidal kinetic energy $\mathcal{E} \equiv 1/(2\Gamma)\int_D(\psi_x^2 + \psi_y^2)dx\,dy$ as a function of Ra in the subcritical and supercritical regimes.

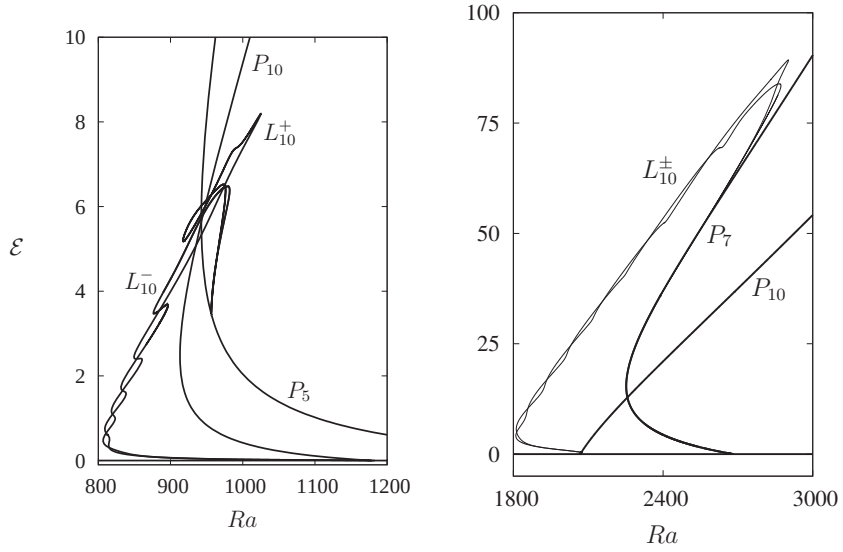

Figure 11: The average poloidal kinetic energy as a function of Ra showing slanted snaking. (a) The subcritical case with $Ta = 20$, $\sigma = 0.1$. (b) The supercritical case with $Ta = 40$, $\sigma = 0.6$. The label P_n refers the periodic solutions with n wavelengths within the domain $\Gamma = 10\lambda_c$; P_{10} bifurcates subcritically in (a) and supercritically in (b). From [1].

The behavior of the snaking region is notably different from that of the Swift–Hohenberg equation that we have seen before: Fig. 11(a) (subcritical) shows that the snaking exists *beyond* the bistability region, and Fig. 11(b) shows that the presence of snaking even in the supercritical case. In both cases, the two intertwined branches form *slanted snaking* [1]. The dramatic change in the snaking scenario is a result of the finite period Γ of the domain together with the conservation of zonal momentum, cf. [5, 11]. In the limit that $\Gamma \to \infty$ or if the free-slip boundary condition is replaced with no-slip boundary conditions, the flux conservation will be lost and snaking is expected to become vertical as in the standard snaking scenario (cf. the Swift-Hohenberg equation).

Figures 12 and 13 present the solution profiles corresponding to Figs. 11(a,b), respectively. These results show that cyclonic shear in the convecton-free zones compensates the anticyclonic shear produced by the convectons and is a consequence of periodic boundary conditions with finite period Γ. The solutions in both cases grow in the same manner as one proceeds up the snaking branches despite the fact that in Fig. 11(b) no distinct nucleation events take place, i.e., no saddle-nodes are present. This type of snaking has been called "smooth snaking" [6].

Slanted snaking is a consequence of the expulsion of shear from the convecton – negative shear implies that the structure rotates more slowly than the frame. Conservation of zonal momentum now implies that the flow outside the convecton must rotate faster, i.e., that the resulting convecton is embedded in a shear layer that it generates for itself. To understand this process in a little more detail we write $Ra = Ra_c + \epsilon^2 r$, where $r = \mathcal{O}(1)$, $\epsilon \ll 1$, and

introduce slow scales $X = \epsilon x$ and $T_2 = \epsilon^2 t$. We look for solutions in the form [4]

$$\psi = \frac{\epsilon}{2}\left(a(X,T_2)e^{ikx} + c.c.\right)\sin(\pi z) + h.o.t., \tag{18}$$

$$\theta = \frac{\epsilon k}{2p}\left(ia(X,T_2)e^{ikx} + c.c.\right)\sin(\pi z) + h.o.t., \tag{19}$$

$$v = \epsilon V(X,T_2) + \frac{\epsilon T\pi}{2p}\left(a(X,T_2)e^{ikx} + c.c.\right)\cos(\pi z) + h.o.t. \tag{20}$$

The large scale zonal velocity V is necessary to capture the shear that builds up across a convecton and enters at $\mathcal{O}(\epsilon)$; its inclusion is a consequence of the phase-like quality of the variable v, i.e., the invariance of Eqs. (12)–(14) with the boundary conditions (15) with respect to $v \to v + c$, where c is a constant. At third order we obtain the equations [4]

$$\frac{p(3k^2\sigma - k^2 + 2\pi^2)}{\sigma k^2}a_{T_2} = ra + 12pa_{XX} - \frac{3pk^2}{8}(1-\xi^2)|a|^2 a - \frac{T\pi^2}{\sigma k^2}aV_X, \tag{21}$$

$$V_{T_2} = \sigma V_{XX} + \frac{T\pi^2}{4p}\left(|a|^2\right)_X, \tag{22}$$

where $\xi \equiv \frac{T\pi^2}{\sqrt{3}pk^2\sigma} > 0$. In rescaled form these equations become

$$\eta A_{T_2} = rA + A_{XX} - \frac{1-\xi^2}{2}|A|^2 A - \xi A V_X, \tag{23}$$

$$V_{T_2} = V_{XX} + \xi\left(|A|^2\right)_X, \tag{24}$$

where $\eta \equiv \frac{3k^2\sigma - k^2 + 2\pi^2}{12k^2}$. The quantity η vanishes at the Takens-Bogdanov point $Ra_H = Ra_c$ where Ra_H is the critical Rayleigh number for the onset of a Hopf mode with the same wavenumber k. In the present work we are interested in the case in which the conduction state loses stability at a steady state bifurcation, i.e., a Hopf bifurcation is absent. In this case $\eta > 0$.

In the stationary case with PBC on the large scale X Eq. (24) implies that

$$V_X = \xi\left(\left\langle|A|^2\right\rangle - |A|^2\right), \tag{25}$$

where $\langle\cdot\rangle$ represents a spatial average over the domain. Thus $V_X > 0$ if $|A|^2 < \left\langle|A|^2\right\rangle$, i.e., outside the convecton, while $V_X < 0$ if $|A|^2 > \left\langle|A|^2\right\rangle$, i.e., inside the convecton, exactly as found in Figs. 12 and 13. Moreover, using Eq. (25) to eliminate V_X from Eq. (23) we obtain the *nonlocal* equation [4]

$$rA + A_{XX} - \frac{1}{2}(1-3\xi^2)|A|^2 A - \xi^2\left\langle|A|^2\right\rangle A = 0. \tag{26}$$

If follows that there are four possible scenarios for the primary–secondary bifurcations with PBC: (1) both bifurcations are subcritical ($\xi^2 > 1$), (2) the primary bifurcation is supercritical while the secondary bifurcation is subcritical ($3/7 < \xi^2 < 1$), (3) both bifurcations are supercritical ($1/3 < \xi^2 < 3/7$), and (4) the primary bifurcation is supercritical but no secondary bifurcation is present ($\xi^2 < 1/3$) [1, 7]. When the domain period Γ is sufficiently

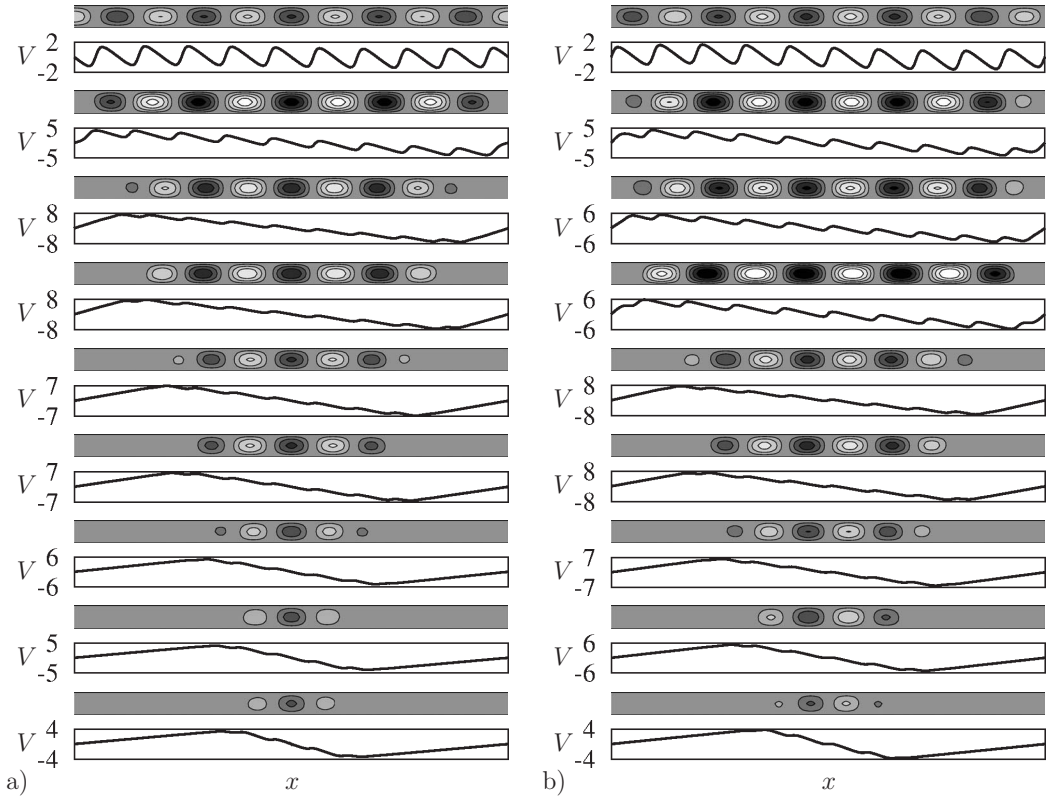

Figure 12: Solution profiles at successive saddle-nodes on (a) L_{10}^{-}, (b) L_{10}^{+} in Fig. 11(a) (subcritical case). Upper panels show the contours of the streamfunction $\psi(x, z)$, and the lower panels show $V(x)$. From [1].

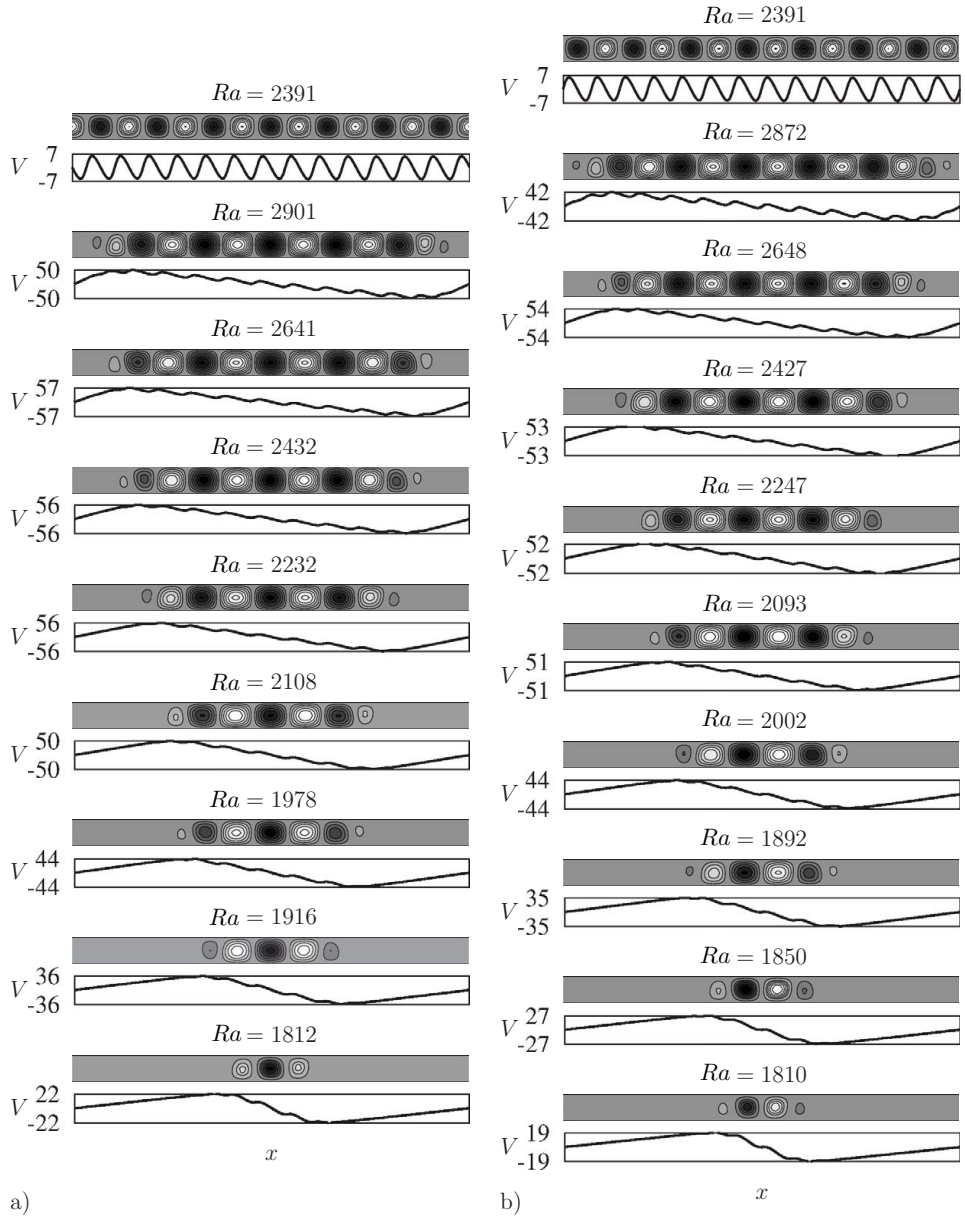

Figure 13: Solution profiles at successive saddle-nodes on (a) L_{10}^{-}, (b) L_{10}^{+} in Fig. 11(b) (supercritical case). Upper panels show the contours of the streamfunction $\psi(x, z)$, and the lower panels show $V(x)$. From [1].

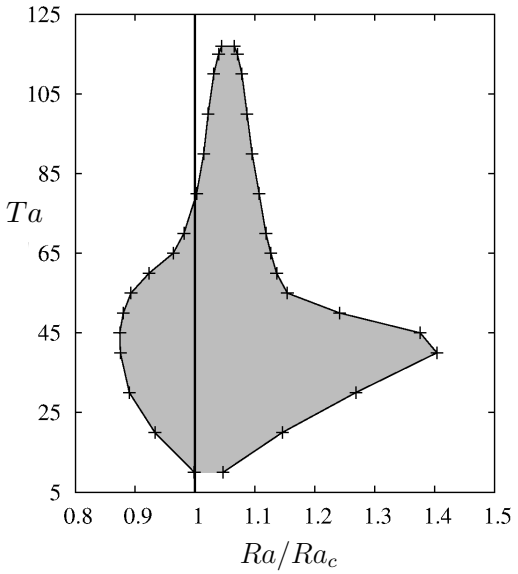

Figure 14: The existence region of convectons in the (Ra, Ta) plane when $\sigma = 0.6$, with the onset of periodic convection marked as a vertical line. From [1].

large the secondary bifurcations that form convectons occur at small enough amplitude that the transitions are captured wall by the abobe asymptotic analysis.

The range of existence of localised states in Ra depends on both the Taylor number Ta and the Prandtl number. For sufficiently large values of Ta, or for values of Ta that are too small, there are no localized states, as shown in Fig. 14. For small values of Ta, there are no localized states because the rotation is too weak for shear expulsion to take place. For $Ta \gtrsim 60$, the wavelength of the localized states decreases significantly, due to the requirements of the Taylor-Proudman theorem and for $Ta \gtrsim 110$ the convectons are sheared out and the average poloidal kinetic energy of the states decreases to zero. Further details and discussion of the effect of changing Ta can be found in [1].

References

C. Beaume, A. Bergeon, H.-C. Kao and E. Knobloch. Convectons in a rotating fluid layer, *J. Fluid Mech.*, in press.

A. Bergeon, J. Burke, E. Knobloch and I. Mercader. Eckhaus instability and homoclinic snaking. *Phys. Rev. E* **78**, 046201, 2008.

J. R. Burke. *Localized States in Driven Dissipative Systems*. PhD thesis, University of California, Berkeley, 2008.

S. M. Cox and P. C. Matthews. New instabilities in two-dimensional rotating convection and magnetoconvection. *Physica D* **149**, pp. 210–229, 2001.

J. H. P. Dawes. Localized pattern formation with a large-scale mode: slanted snaking. *SIAM J. Appl. Dyn. Sys.* **7**, pp. 18–206, 2008.

J. H. P. Dawes and S. Lilley. Localized states in a model of pattern formation in a vertically vibrated layer. *SIAM J. Appl. Dyn. Sys.* **9**, pp. 238–260, 2010.

F. J. Elmer. Nonlinear and nonlocal dynamics of spatially extended systems: Stationary states, bifurcations and stability. *Physica D* **30**, pp. 321–342, 1988.

S. Houghton and E. Knobloch. Swift-Hohenberg equation with broken cubic-quintic nonlinearity. *Phys. Rev. E* **84**, 016204, 2011.

J. Knobloch, D. J. B. Lloyd, B. Sandstede and T. Wagenknecht. Isolas of 2-pulse solutions in homoclinic snaking scenarios. *J. Dyn. Diff. Eq.* **23**, 93–114, 2011.

D. Lo Jacono, A. Bergeon and E. Knobloch. Spatially localized binary fluid convection in a porous medium. *Phys. Fluids* **22**, 073601, 2010.

D. Lo Jacono, A. Bergeon and E. Knobloch. Spatially localized magnetoconvection. *J. Fluid Mech.* **687**, pp. 595–605, 2011.

I. Mercader, O. Batiste, A. Alonso and E. Knobloch. Travelling convectons in binary fluid convection. *J. Fluid Mech.*, under review.

G. Veronis. Large-amplitude Bénard convection in a rotating fluid, *J. Fluid Mech.* **31**, pp. 113–139, 1968.